

Cite this: *Dalton Trans.*, 2024, **53**, 15509

# Nitrogen-doped carbon layer coated Co(OH)F/CoP<sub>2</sub> nanosheets for high-current hydrogen evolution reaction in alkaline freshwater and seawater†‡

Yuxuan Wang,‡ Chao Fan,‡ Kang Wang and Yan-Qin Wang \*

Utilizing renewable energy such as offshore wind power to electrolyze seawater for hydrogen production offers a sustainable development pathway to address energy and climate change issues. In this study, by incorporating nitrogen-doped carbon quantum dots (N-CDs) into precursors, we successfully synthesized a nitrogen-doped carbon (NC)-layer-coated Co(OH)F/CoP<sub>2</sub> catalyst NC@Co(OH)F/CoP<sub>2</sub>/NF loaded on nickel foam (NF). The introduction of N-CDs induced significant morphology change of the catalyst, facilitating the exposure of numerous active sites, ensuring the presence of catalytically active species CoP<sub>2</sub> in nanoparticle form and avoiding agglomeration, which was advantageous to enhancing the overall hydrogen evolution reaction (HER) activity of the catalyst. The formation of Co–N bonds accelerated electron transfer, regulated the electronic structure, and optimized the catalyst's adsorption capacity for H\* intermediates, which resulted in remarkably improved HER performance. In addition, Co(OH)F can also serve as a structural support, preventing the catalyst from collapsing during the HER catalytic process. NC@Co(OH)F/CoP<sub>2</sub>/NF exhibited excellent HER activity in alkaline freshwater and alkaline seawater, respectively requiring overpotentials of only 107 and 128 mV to achieve a current density of 100 mA cm<sup>-2</sup>. More importantly, it also demonstrated excellent HER activity at high current densities, with overpotentials of 189 and 237 mV at a current density of 1000 mA cm<sup>-2</sup> in alkaline freshwater and alkaline seawater, respectively. This work provides new insights into the design and construction of highly efficient HER catalysts for applications in alkaline freshwater and seawater.

Received 12th June 2024,  
Accepted 2nd September 2024

DOI: 10.1039/d4dt01713g

rsc.li/dalton

## Introduction

To address energy and climate change issues, the utilization of renewable energy for electrolyzing water to produce high-purity hydrogen gas (H<sub>2</sub>) provides a sustainable pathway.<sup>1,2</sup> Commonly used electrolyzers such as proton exchange membrane water electrolyzer (PEMWE), alkaline water electrolyzer (AWE), and anion exchange membrane water electrolyzer (AEMWE) typically employ high-purity fresh water as feedstock.<sup>3–6</sup> However, the limited availability of freshwater could become a bottleneck for large-scale hydrogen production. Pure water, as a common electrolyte, possesses a low electrical conductivity, thus necessitating the addition of phosphate buffer solutions, potassium hydroxide, or sulfuric acid to enhance the conductivity of the electrolyte. In contrast, seawater, due to its higher salinity, exhibits higher electrical

conductivity compared to pure water. Therefore, the integration of ocean-related green energy technologies, such as offshore wind power generation coupled with seawater electrolysis, represents one of the most promising pollution-free approaches for H<sub>2</sub> production.<sup>7,8</sup> Nevertheless, electrolyzing seawater faces additional challenges: seawater contains a plethora of impurities such as metal ions (Mg<sup>2+</sup>, Ca<sup>2+</sup>, etc.), bacteria, and microorganisms.<sup>9</sup> During seawater electrolysis, these impurities can cause electrode fouling, thereby poisoning or accelerating the aging of electrodes and catalysts in the electrolysis system, rendering them unable to operate stably for long periods or even losing activity.<sup>10</sup> For instance, when noble metals are used as hydrogen evolution reaction (HER) electrocatalysts, the highly corrosive hypochlorite byproduct generated near the electrode can block the active sites of noble metal catalysts.<sup>11–13</sup> To enable wider applications, it is imperative to develop efficient and stable non-noble metal electrocatalysts.

Transition metal compounds such as nitrides, carbides, sulfides, and phosphides have attracted widespread attention due to their unique properties.<sup>14–20</sup> Among them, transition metal phosphides (TMPs) exhibit enhanced conductivity and resistance to chloride corrosion, making them promising

Inner Mongolia Key Laboratory of Rare Earth Catalysis, College of Chemistry and Chemical Engineering, Inner Mongolia University, Huhhot, 010021, China.

E-mail: yqwang\_chem@imu.edu.cn; Fax: +86-471-4994375; Tel: +86-471-4994375

† Electronic supplementary information (ESI) available. See DOI: <https://doi.org/10.1039/d4dt01713g>

‡ These authors contributed equally.

catalysts.<sup>21–25</sup> Tian *et al.* reported the surface-layer-confined boron doping on cobalt phosphide nanowire arrays (B-CoP) *via* a controllable surface redox reaction. B-doping induced electron redistribution of Co with electron-rich features, which optimizes  $\Delta G_{\text{H}^+}$  and thereby accelerating reaction kinetics. B-CoP exhibited excellent HER catalytic activity.<sup>26</sup> Huang *et al.* reported a cobalt phosphide–cobalt oxide composite catalyst (CoP–Co<sub>x</sub>O<sub>y</sub>/CC) supported on carbon cloth, which exhibited good activity and durability toward HER in alkaline medium. Theoretical studies verified that the redistribution of electrons at laterally dispersed Co phosphide/oxide interfaces gave rise to a synergistic effect in the heterostructured composite. Through the synergistic effect in the composite, various Co oxide phases initiate the dissociation of the alkaline water molecule. Moreover, the highly active CoP further facilitates the adsorption–desorption process of water electrolysis, leading to extremely high HER activity.<sup>27</sup> Most of the cobalt phosphide species reported in the literature are focused on CoP.<sup>28</sup> Literature has indicated that the HER catalytic activity of cobalt phosphide increases with the P content. Therefore, CoP<sub>2</sub> with a high phosphorus content has great potential as a hydrogen evolution catalyst.<sup>29</sup> In addition, carbon-based materials are widely used as electrode materials due to their simple synthesis, good conductivity, and corrosion resistance.<sup>30–32</sup> Carbon dots (CDs), as a novel type of carbon-based material with abundant functional groups, can bond with metal ions, simultaneously regulating the morphology of the material and inhibiting the aggregation of nanoparticles, thus facilitating the exposure of more active sites.<sup>33</sup> Moreover, the carbon layer derived from carbon dots can serve as armor, protecting the internal catalysts from corrosion and enhancing the conductivity of the material.<sup>34–36</sup> If carbon-based materials are combined with TMPs, the catalytic performance of TMPs is expected to be improved.

Herein, we employed nitrogen-doped carbon dots (N-CDs) as structure-promoting agents to disperse and stabilize CoP<sub>2</sub> nanoparticles. By utilizing hydrothermal and chemical vapor deposition (CVD) phosphorization, we successfully prepared a catalyst NC@Co(OH)F/CoP<sub>2</sub>/NF which consisted of NC-layer-coated Co(OH)F/CoP<sub>2</sub> nanoparticles on nickel foam (NF) substrates. The introduction of N-CDs can modulate the morphology of the catalyst precursor, facilitating the exposure of more active sites. Subsequently formed conductive NC layers can protect the internal catalyst, preventing the dissolution of the catalyst during the electrolysis process. Meanwhile, the electron transfer between the NC layers and the dispersed metal phosphides effectively adjusts the electron structure around the active centers, thereby enhancing the HER catalytic performance. Moreover, Co(OH)F species are highly stable during the HER process, providing a support to the catalyst and preventing its collapse. Electrochemical test results demonstrated that NC@Co(OH)F/CoP<sub>2</sub>/NF exhibited excellent HER catalytic activity in 1.0 M KOH and natural seawater containing 1.0 M KOH, with overpotentials of only 107 and 128 mV, respectively, at a current density of 100 mA cm<sup>-2</sup>. Importantly, it also displays excellent HER activity at high

current densities, with overpotentials of only 189 and 237 mV even at a current density of 1000 mA cm<sup>-2</sup>.

## Experimental

### Materials and methods

Ni foam was purchased from Kunshan Baiyida Electronic New Materials Co., Ltd. KOH was purchased from Shanghai Maclin Biochemical Technology Co., Ltd. Natural seawater was obtained from the Bohai Sea in China. Urea was purchased from Tianjin Xinbote Chemical Co., Ltd. Citric acid, ethylenediamine, Co(NO<sub>3</sub>)<sub>2</sub>·6H<sub>2</sub>O, NaH<sub>2</sub>PO<sub>4</sub>·H<sub>2</sub>O, and NH<sub>4</sub>F were purchased from Beijing Chemical Works. All chemicals and materials were not processed for further purification and treatment. X-ray diffraction (XRD) measurements were performed using a Rigaku Ultima IV diffractometer at a scanning rate of 0.013° in the Bragg angle range from 5° to 80° with Cu K $\alpha$  radiation ( $\lambda = 1.5418 \text{ \AA}$ ). X-ray photoelectron spectroscopy (XPS) measurements were performed using an ESCALAB XI+. All spectra were calibrated using the C–C peak of C 1s orbitals as 284.8 eV. Scanning electron micrographs were performed using a Regulus 8100 field emission scanning electron microscope (FE-SEM). Transmission electron microscopy (TEM) was performed using a Tecnai G2 F30 field-emission transmission electron microscope (FE-TEM). Fourier transform infrared (FTIR) spectra were measured by a Spectrum Two infrared spectrometer. Inductively coupled plasma-optical emission spectroscopy (ICP-OES) was measured by Agilent 725.

### Synthesis of N-CDs

Using a typical synthesis method, 1.84 g of citric acid and 0.6 g of ethylenediamine were dissolved in 17 mL of deionized water and stirred at room temperature for 15 minutes. Subsequently, the solution was transferred into a 30 mL high-pressure reaction vessel and heated at 200 °C for 8 hours. After naturally cooling to room temperature, the mixture was centrifuged to remove the precipitate. The collected brown liquid was then subjected to freeze drying for 48 hours in a freeze dryer to obtain N-CDs.<sup>37</sup>

### Synthesis of NC@Co(OH)F/Co(OH)(CO<sub>3</sub>)<sub>0.5</sub>/NF

NF (2 cm × 2 cm) was successively cleaned with 1 M HCl, acetone, ethanol, and deionized water for 15 minutes each. 0.52 g of Co(NO<sub>3</sub>)<sub>2</sub>·6H<sub>2</sub>O, 0.53 g of urea, 0.28 g of NH<sub>4</sub>F, and 0.04 g of N-CDs powder were dissolved in 17 mL of deionized water and stirred at room temperature for 15 minutes. Then, the above solution was transferred to a 30 mL Teflon-steel autoclave, and the pretreated NF was suspended vertically in the solution. Subsequently, the Teflon-steel autoclave was maintained at 120 °C for 10 hours. After naturally cooling to room temperature, the product was washed several times with deionized water and anhydrous ethanol to remove surface residual ions. The resulting product obtained after drying at room temperature was named NC@Co(OH)F/Co(OH)(CO<sub>3</sub>)<sub>0.5</sub>/NF.

### Synthesis of NC@Co(OH)F/NF

The synthesis of NC@Co(OH)F/NF was similar to that of NC@Co(OH)F/Co(OH)(CO<sub>3</sub>)<sub>0.5</sub>/NF, except that urea was not added.

### Synthesis of NC@Co(OH)F/CoP<sub>2</sub>/NF

In the typical phosphorization process, a quartz boat containing 1.0 g of NaH<sub>2</sub>PO<sub>2</sub>·H<sub>2</sub>O was placed upstream in a tubular furnace as the phosphorus source, while a quartz boat containing NC@Co(OH)F/Co(OH)(CO<sub>3</sub>)<sub>0.5</sub>/NF was placed downstream. Then, under N<sub>2</sub> protection, the temperature was ramped up to 350 °C at a rate of 3 °C min<sup>-1</sup> and held for 2 hours. The resulting product was named NC@Co(OH)F/CoP<sub>2</sub>/NF.

### Synthesis of Co(OH)F/Co(OH)(CO<sub>3</sub>)<sub>0.5</sub>/NF

The synthesis of Co(OH)F/Co(OH)(CO<sub>3</sub>)<sub>0.5</sub>/NF was similar to that of NC@Co(OH)F/Co(OH)(CO<sub>3</sub>)<sub>0.5</sub>/NF, except that N-CDS were not added.

### Synthesis of Co(OH)F/CoP<sub>2</sub>/NF

The synthesis of Co(OH)F/CoP<sub>2</sub>/NF was similar to that of NC@Co(OH)F/CoP<sub>2</sub>/NF, except that the precursor was replaced by Co(OH)F/Co(OH)(CO<sub>3</sub>)<sub>0.5</sub>/NF.

### Electrochemical measurements

All electrochemical measurements were carried out using a CHI660E electrochemical workstation with a three-electrode electrochemical system in 1.0 M KOH or natural seawater containing 1.0 M KOH solution at room temperature. A carbon rod was used as the counter electrode for all tests, the reference electrode was an Ag/AgCl electrode, and the working electrode was a 1 cm × 1 cm electrocatalyst. Linear sweep voltammetry (LSV) polarization curves in the voltage range of -0.8 to -3.0 V vs. Ag/AgCl for HER were conducted at a scan rate of 5 mV s<sup>-1</sup>. The accelerated durability tests (ADTs) were conducted for 3000 CV (cyclic voltammetry) cycles. Electrochemical impedance spectroscopy (EIS) was performed at an overpotential of 0.284 V vs. RHE for HER over the frequency range from 100 kHz to 0.1 Hz. The electrochemical surface areas (ECSAs) were obtained from the double-layer capacitance (C<sub>dl</sub>). The ECSAs were measured at voltages from 0.23 to 0.33 V vs. RHE by CV tests with various scan rates ranging from 20 mV s<sup>-1</sup> to 100 mV s<sup>-1</sup>.

## Results and discussion

### Synthesis and structural characterization

As shown in Fig. 1a, NC@Co(OH)F/CoP<sub>2</sub>/NF electrocatalyst was synthesized through hydrothermal and chemical vapor deposition (CVD) phosphorization methods. Initially, vertically aligned nanosheet arrays of NC@Co(OH)F/Co(OH)(CO<sub>3</sub>)<sub>0.5</sub> were constructed on the surface of NF substrate after hydrothermal reaction. Subsequently, under N<sub>2</sub> atmosphere and phosphorization treatment, the Co-containing species were selectively phosphorized into CoP<sub>2</sub>, and the resulting final

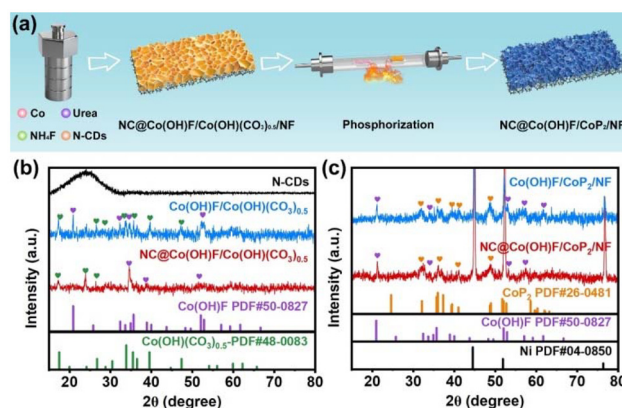


**Fig. 1** (a) Schematic diagram of the preparation process of NC@Co(OH)F/CoP<sub>2</sub>/NF, (b) XRD patterns of N-CDS, Co(OH)F/Co(OH)(CO<sub>3</sub>)<sub>0.5</sub> and NC@Co(OH)F/Co(OH)(CO<sub>3</sub>)<sub>0.5</sub>; standard PDF cards for Co(OH)F and Co(OH)(CO<sub>3</sub>)<sub>0.5</sub>, (c) XRD patterns of Co(OH)F/CoP<sub>2</sub>/NF and NC@Co(OH)F/CoP<sub>2</sub>/NF; standard PDF cards for CoP<sub>2</sub>, Co(OH)F, and Ni.

product was NC@Co(OH)F/CoP<sub>2</sub>/NF. The characterization of N-CDS was conducted by using an FTIR spectrometer, as shown in Fig. S1.† The peaks located at 3250 and 2924 cm<sup>-1</sup> were attributed to the stretching vibrations of O–H and C–H bonds, respectively, while the peak at 1658 cm<sup>-1</sup> was assigned to the vibration of C=O bonds. The peak at 1156 cm<sup>-1</sup> could be attributed to the asymmetric stretching vibration of C–NH–C bonds.<sup>38</sup> Notably, N-CDS contain various functional groups, enabling them to bond with metal ions during the preparation process of catalysts.<sup>39</sup> Upon irradiation with ultraviolet light, the N-CDS solution, where the N-CDS were mixed with de-ionized water, exhibited blue fluorescence, further confirming the successful preparation of N-CDS.<sup>40</sup> As shown in Fig. 1b, the powder XRD patterns of NC@Co(OH)F/Co(OH)(CO<sub>3</sub>)<sub>0.5</sub> and Co(OH)F/Co(OH)(CO<sub>3</sub>)<sub>0.5</sub> were obtained from the residual products in the autoclave during the synthesis of NC@Co(OH)F/Co(OH)(CO<sub>3</sub>)<sub>0.5</sub>/NF and Co(OH)F/Co(OH)(CO<sub>3</sub>)<sub>0.5</sub>/NF. Regardless of the presence of N-CDS, the XRD patterns exhibit diffraction peaks corresponding to both Co(OH)F (JCPDS no. 50-0827) and Co(OH)(CO<sub>3</sub>)<sub>0.5</sub> (JCPDS no. 48-0083) phases. However, when N-CDS are present, the decreases in the intensity of some diffraction peaks of Co(OH)F and Co(OH)(CO<sub>3</sub>)<sub>0.5</sub> are observed. Additionally, no peak corresponding to carbon is detected compared to pristine N-CDS. This may be attributed to the transformation of N-CDS into amorphous NC layers after hydrothermal treatment, with a relatively lower content and amorphous nature.<sup>41,42</sup> After phosphorization treatment, the XRD patterns of the catalysts loaded on NF (Fig. 1c) reveal new peaks corresponding to CoP<sub>2</sub> (JCPDS no. 26-0481), while the diffraction peaks of Co(OH)(CO<sub>3</sub>)<sub>0.5</sub> disappear, and those of Co(OH)F remain. Therefore, it is inferred that during the phosphorization process of the catalyst, the difference in stability between Co(OH)F and Co(OH)(CO<sub>3</sub>)<sub>0.5</sub> results in the preferential transformation of Co(OH)(CO<sub>3</sub>)<sub>0.5</sub> into CoP<sub>2</sub>, while Co(OH)F is retained. Consequently, the final product obtained is the NC layer-coated Co(OH)F/CoP<sub>2</sub> catalyst loaded on NF.

Fig. 2 and Fig. S2† show the SEM images of each catalyst at different magnifications. When N-CDs are not added, the precursor exhibits aggregated nanoneedle morphology (Fig. S2a and c†), while after the addition of N-CDs (Fig. S2b and d†), it transforms into stacked nanosheet morphology. This indicates that the introduction of N-CDs can adjust the morphology of the precursor. When the precursor without N-CDs is phosphorized (Fig. 2a and c), the surface morphology of the catalyst remains unchanged compared to that before phosphorization. However, for the precursor containing N-CDs (Fig. 2b and d), the phosphorization treatment induces a significant change in the morphology of the catalyst, displaying stacked nanosheets with rough edges and increased exposed active surface. This phenomenon may be attributed to the transformation of N-CDs into an amorphous NC layer, which changed the catalyst's morphology. Meanwhile, the remaining un-phosphorized Co(OH)F acts as a structure support, maintaining the catalyst structure.

Furthermore, the structure of NC@Co(OH)F/CoP<sub>2</sub>/NF was also investigated by using TEM. As shown in Fig. 3a, numerous

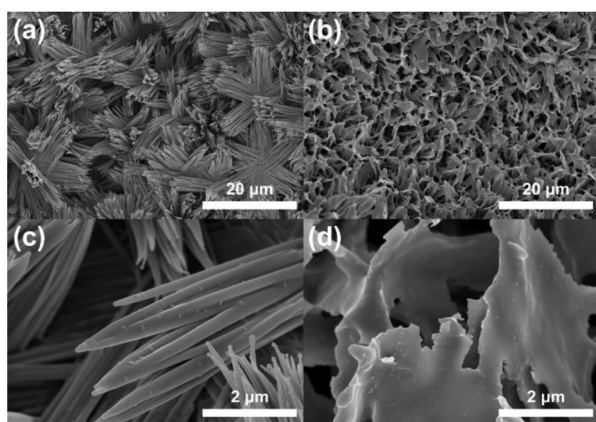


Fig. 2 SEM images of catalysts at different magnifications. (a and c) Co(OH)F/CoP<sub>2</sub>/NF and (b and d) NC@Co(OH)F/CoP<sub>2</sub>/NF.

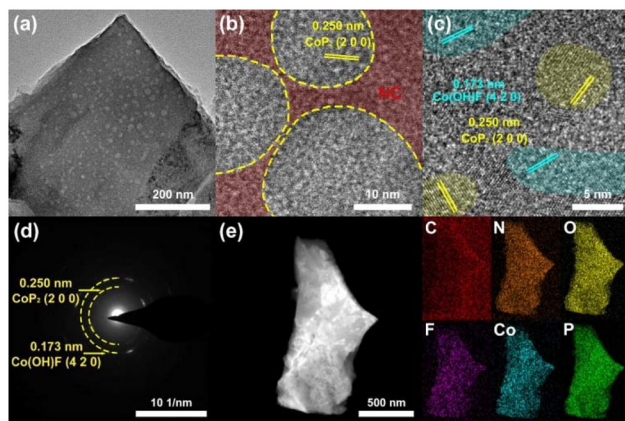


Fig. 3 TEM image (a), HR-TEM images (b and c), SAED pattern (d), mapping images of NC@Co(OH)F/CoP<sub>2</sub>/NF (e).

spots distributed on the nanosheets were observed, which were identified as nanoscale particles. High-resolution transmission electron microscopy (HR-TEM) was applied to measure the lattice spacings (Fig. 3b and c), the lattice spacing of 0.250 nm corresponds to the (2 0 0) crystal plane of CoP<sub>2</sub>, which also corresponds to the diffraction peak at 35.8° in the XRD pattern. The lattice spacing of 0.173 nm corresponds to the (4 2 0) crystal plane of Co(OH)F, which also corresponds to the diffraction peak at 52.7° in the XRD pattern. No lattice fringes were found for the nanoscale spots, suggesting the presence of amorphous NC layer formed by the transformation of N-CDs. Fig. 3d presents the selected area electron diffraction (SAED) pattern, showing two concentric rings at 0.173 and 0.250 nm, confirming the coexistence of the (4 2 0) crystal plane of Co(OH)F and the (2 0 0) crystal plane of CoP<sub>2</sub>. Additionally, the elemental mapping images (Fig. 3e) indicate the uniform distribution of C, N, O, F, Co, and P elements in the catalyst.

Furthermore, XPS was utilized to analyze the elemental valence states and electronic structure of the catalyst surface. As shown in Fig. S3,† the XPS survey spectra for NC@Co(OH)F/Co(OH)(CO<sub>3</sub>)<sub>0.5</sub>/NF, Co(OH)F/CoP<sub>2</sub>/NF, and NC@Co(OH)F/CoP<sub>2</sub>/NF reveal the presence of Co, F, O, N, C, and P elements. In the spectrum of Co(OH)F/CoP<sub>2</sub>/NF, no characteristic peak signal of nitrogen (N) is observed, while in the spectrum of NC@Co(OH)F/Co(OH)(CO<sub>3</sub>)<sub>0.5</sub>/NF, no characteristic peak signal of P is observed. Additionally, in the spectra of NC@Co(OH)F/Co(OH)(CO<sub>3</sub>)<sub>0.5</sub>/NF and NC@Co(OH)F/CoP<sub>2</sub>/NF, the characteristic peak signal of C is stronger than that of Co(OH)F/CoP<sub>2</sub>/NF, which is attributed to the additional introduction of carbon originated from carbon quantum dots in the system. The high-resolution XPS spectra of C 1s are shown in Fig. 4a. For NC@Co(OH)F/CoP<sub>2</sub>/NF, the peaks located at 284.8 eV, 285.9 eV, 287.1 eV, and 289.0 eV can be identified as C-C/C=C, C-O, C-N, and N-C=O, respectively, similar to the

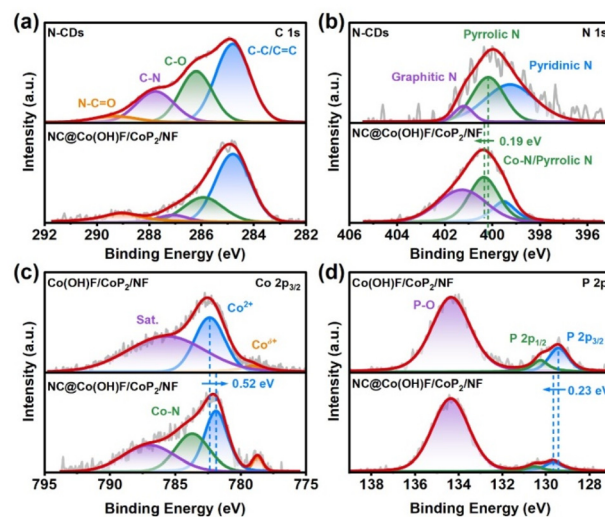
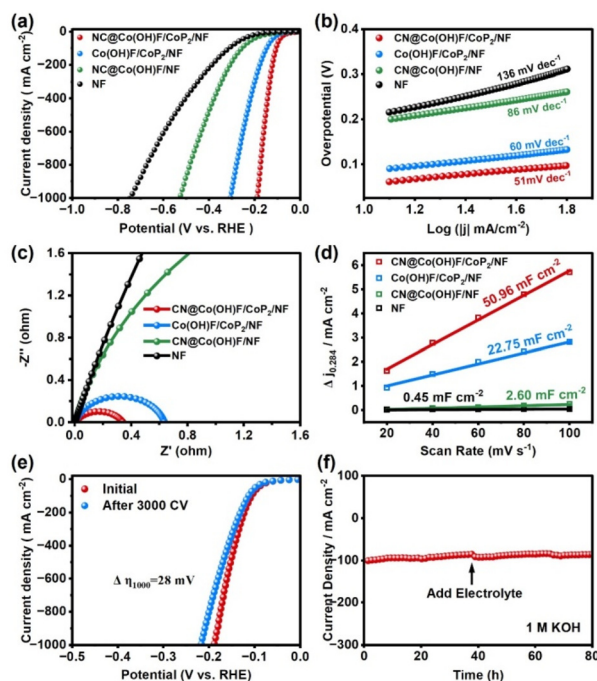


Fig. 4 XPS spectra for (a) C 1s, (b) N 1s, (c) Co 2p<sub>3/2</sub>, and (d) P 2p, respectively.

corresponding peak attribution in the original N-CDs spectrum.<sup>38,43</sup> In the N 1s spectrum of NC@Co(OH)F/CoP<sub>2</sub>/NF (Fig. 4b), three peaks at 399.5, 400.3, and 401.3 eV correspond to pyridinic N, Co–N/pyrrolic N, and graphitic N, respectively.<sup>44</sup> Notably, compared to N-CDs, NC@Co(OH)F/CoP<sub>2</sub>/NF exhibits a positive shift of 0.19 eV in the N 1s spectrum, attributed to the coupling between the NC layer and Co(OH)F/CoP<sub>2</sub>/NF. After phosphorization at 350 °C, the proportion of graphitic N in NC@Co(OH)F/CoP<sub>2</sub>/NF significantly increases, induced by the high-temperature reaction, leading to changes in the content of different nitrogen-containing species.<sup>45</sup> The high-resolution XPS spectra of Co 2p<sub>3/2</sub> are shown in Fig. 4c. For NC@Co(OH)F/CoP<sub>2</sub>/NF, the peak at 778.7 eV can be attributed to Co<sup>δ+</sup>.<sup>46</sup> The peaks at 781.9 and 787.0 eV belong to Co<sup>2+</sup> and satellite peaks, respectively. Compared to Co(OH)F/CoP<sub>2</sub>/NF, a new peak appears at 783.7 eV corresponding to the Co–N bond, indicating the coupling between Co species and the NC layer, generating a Co–N charge transfer channel.<sup>47,48</sup> Compared to Co(OH)F/CoP<sub>2</sub>/NF, the Co 2p<sub>3/2</sub> of NC@Co(OH)F/CoP<sub>2</sub>/NF is negatively shifted by 0.52 eV, indicating that the formation of Co–N bonds can promote electron transfer and regulates the electronic structure, which may optimize the catalyst's adsorption capacity for H<sup>+</sup> intermediates, thereby improving catalytic performance. In the P 2p spectrum of NC@Co(OH)F/CoP<sub>2</sub>/NF (Fig. 4d), two weak peaks at 129.6 and 130.5 eV correspond to P 2p<sub>3/2</sub> and P 2p<sub>1/2</sub>, respectively, while the strong peak at 134.4 eV corresponds to the P–O bond, attributed to exposure of the catalyst to air.<sup>49,50</sup> Compared to Co(OH)F/CoP<sub>2</sub>/NF, the P 2p of NC@Co(OH)F/CoP<sub>2</sub>/NF is positively shifted by 0.23 eV, further confirming the interaction between CoP<sub>2</sub> and the NC layer. The O 1s spectrum of NC@Co(OH)F/CoP<sub>2</sub>/NF (Fig. S4a†) exhibits peaks at 531.9 and 533.3 eV corresponding to P–O and –OH groups, respectively. Fig. S4b† shows the high-resolution XPS spectrum of F 1s.

The HER performance was tested in 1.0 M KOH using a typical three-electrode system, with a 95% IR compensation. Fig. 5a displays the LSV curves of NC@Co(OH)F/CoP<sub>2</sub>/NF, Co(OH)F/CoP<sub>2</sub>/NF, NC@Co(OH)F/NF, and NF. It can be found that NC@Co(OH)F/CoP<sub>2</sub>/NF exhibits the highest HER activity among all the catalysts. At a current density of 100 mA cm<sup>-2</sup>, NC@Co(OH)F/CoP<sub>2</sub>/NF shows an overpotential of only 107 mV, lower than the other reference samples Co(OH)F/CoP<sub>2</sub>/NF (149 mV), NC@Co(OH)F/NF (258 mV), and NF (314 mV). Furthermore, at a current density of 1000 mA cm<sup>-2</sup>, the overpotential of NC@Co(OH)F/CoP<sub>2</sub>/NF is only 189 mV, also lower than the other reference samples Co(OH)F/CoP<sub>2</sub>/NF (307 mV), NC@Co(OH)F/NF (530 mV), and NF (748 mV). We also compared the catalytic activity of recently reported catalysts for HER in 1.0 M KOH electrolyte (Table S1†), which demonstrates the excellent HER activity of NC@Co(OH)F/CoP<sub>2</sub>/NF. The presence of the NC layer can disperse CoP<sub>2</sub> nanoparticles well, expose active edge sites, and prevent aggregation during the catalytic process, thereby improving the HER catalytic performance.<sup>51</sup> As shown in Fig. 5b, to further explore the reaction kinetics of the catalysts, the Tafel slopes of the reference catalysts were fitted using the Tafel equation. It was found that



**Fig. 5** The electrochemical HER performance of the catalysts in 1.0 M KOH. (a) LSV curves, (b) Tafel plots, (c) Nyquist plots, (d)  $C_{dl}$  values at 0.284 V vs. RHE of all the reference catalysts, (e) LSV curves of NC@Co(OH)F/CoP<sub>2</sub>/NF before and after 3000 CV cycles, (f)  $i-t$  test of NC@Co(OH)F/CoP<sub>2</sub>/NF at 100 mA cm<sup>-2</sup>.

NC@Co(OH)F/CoP<sub>2</sub>/NF has the smallest Tafel slope (51 mV dec<sup>-1</sup>), lower than the other reference samples Co(OH)F/CoP<sub>2</sub>/NF (60 mV dec<sup>-1</sup>), NC@Co(OH)F/NF (86 mV dec<sup>-1</sup>), and NF (136 mV dec<sup>-1</sup>), indicating the superior reaction existence of the NC layer accelerates the electron transfer with CoP<sub>2</sub>, regulates the electronic structure of CoP<sub>2</sub>, and optimizes the adsorption of H<sup>+</sup>, thereby accelerating the HER reaction kinetics.<sup>52</sup> Electrochemical impedance spectroscopy (EIS) was used to evaluate the charge transfer resistance ( $R_{ct}$ ). As shown in Fig. 5c and S5†, the  $R_{ct}$  of NC@Co(OH)F/CoP<sub>2</sub>/NF is 0.34  $\Omega$ , lower than that of Co(OH)F/CoP<sub>2</sub>/NF (0.63  $\Omega$ ), NC@Co(OH)F/NF (6.74  $\Omega$ ), and NF (33.31  $\Omega$ ). It indicates that after both the phosphorization treatment and the introduction of the NC layer, the charge transfer resistance of the catalyst NC@Co(OH)F/CoP<sub>2</sub>/NF can be significantly decreased, accelerating the reaction rate at the interface.<sup>53</sup> Moreover, to further investigate the mechanism of the enhanced activity of the catalyst, electrochemical double-layer capacitance ( $C_{dl}$ ) was obtained through cyclic voltammetry (CV) tests in the non-faradaic potential range at different scan rates (20–100 mV s<sup>-1</sup>) to estimate the electrochemical active surface area (ECSA) (Fig. S6†). The calculation method of the ECSA values of the catalysts is given in the ESI.† The results show that NC@Co(OH)F/CoP<sub>2</sub>/NF has the largest ECSA value (1274 cm<sup>2</sup>), which is higher than that of other reference samples: Co(OH)F/CoP<sub>2</sub>/NF (568.75 cm<sup>2</sup>), NC@Co(OH)F/NF (65 cm<sup>2</sup>), and NF (11.25 cm<sup>2</sup>). The enhanced ECSA of NC@Co(OH)F/CoP<sub>2</sub>/NF is attributed to the incomplete

phosphorization which increases the surface roughness of the catalyst, leading to a significant increase in the electrochemical active surface area, and significantly increasing the contact area between the catalyst and the electrolyte.<sup>54</sup> Moreover, as shown in Fig. 5e and f, the cyclic stability and *i*-*t* durability of NC@Co(OH)F/CoP<sub>2</sub>/NF in 1.0 M KOH were also further tested. The results indicate that NC@Co(OH)F/CoP<sub>2</sub>/NF exhibits only a 28 mV increase in overpotential after 3000 cycles of CV testing, and can operate stably for at least 80 hours at a current density of 100 mA cm<sup>-2</sup>. Additionally, we also tested the stability of the catalyst without the NC layer (Co(OH)F/CoP<sub>2</sub>/NF) in 1.0 M KOH. As shown in Fig. S7,† Co(OH)F/CoP<sub>2</sub>/NF exhibited a performance decline of 29 mA cm<sup>-2</sup> for HER after only 45 hours, indirectly confirming that the NC layer in NC@Co(OH)F/CoP<sub>2</sub>/NF serves as a protective shell. To eliminate the influence of ECSA on the catalytic activity of the catalysts, and obtain a more accurate assessment of the intrinsic activity of the catalysts, the ECSA-normalized LSV curves were further tested and analyzed (Fig. S8†). The results show that NC@Co(OH)F/CoP<sub>2</sub>/NF exhibits the most superior intrinsic activity among all the catalysts.<sup>55,56</sup>

Due to the excellent performance of NC@Co(OH)F/CoP<sub>2</sub>/NF in alkaline freshwater containing 1.0 M KOH, we are also inspired to further evaluate its HER performance in natural seawater containing 1.0 M KOH. Fig. 6a presents the LSV curves of NC@Co(OH)F/CoP<sub>2</sub>/NF, Co(OH)F/CoP<sub>2</sub>/NF, NC@Co(OH)F/NF, and NF in natural seawater containing 1.0 M KOH, which indicates that NC@Co(OH)F/CoP<sub>2</sub>/NF still exhibits the highest HER activity among all the reference catalysts. At a current density of 100 mA cm<sup>-2</sup>, NC@Co(OH)F/CoP<sub>2</sub>/NF shows an overpotential of only 128 mV, lower than that of the other reference samples Co(OH)F/CoP<sub>2</sub>/NF (179 mV), NC@Co(OH)F/NF (295 mV), and NF (327 mV). Furthermore, even at a large

current density of 1000 mA cm<sup>-2</sup>, the overpotential of NC@Co(OH)F/CoP<sub>2</sub>/NF is as low as 237 mV, also lower than that of the other reference samples Co(OH)F/CoP<sub>2</sub>/NF (379 mV), NC@Co(OH)F/NF (598 mV), and NF (834 mV). As shown in Fig. 6b, NC@Co(OH)F/CoP<sub>2</sub>/NF displays the smallest Tafel slope (68 mV dec<sup>-1</sup>) among all the samples, lower than that of the other reference samples Co(OH)F/CoP<sub>2</sub>/NF (83 mV dec<sup>-1</sup>), NC@Co(OH)F/NF (109 mV dec<sup>-1</sup>), and NF (181 mV dec<sup>-1</sup>), indicating its optimal reaction kinetics and reaction rate. Furthermore, as shown in Fig. 6c and d, CV cycling stability and *i*-*t* durability of NC@Co(OH)F/CoP<sub>2</sub>/NF in natural seawater containing 1.0 M KOH were also tested. The results indicate that after 3000 cycles of CV testing, NC@Co(OH)F/CoP<sub>2</sub>/NF exhibits a relatively big HER performance decrease of 48 mV in alkaline natural seawater compared to that in freshwater containing 1.0 M KOH. The big HER performance decrease of NC@Co(OH)F/CoP<sub>2</sub>/NF may be induced by the presence of more impurities in seawater, which can corrode the catalyst and cause performance degradation.<sup>57</sup> Moreover, the *i*-*t* test demonstrates that NC@Co(OH)F/CoP<sub>2</sub>/NF can operate stably for at least 40 hours at a current density of 100 mA cm<sup>-2</sup>, indicating the excellent stability of NC@Co(OH)F/CoP<sub>2</sub>/NF. The comparison of HER performance in natural seawater containing 1.0 M KOH between NC@Co(OH)F/CoP<sub>2</sub>/NF and other non-precious metal-based HER electrocatalysts is given in Table S2,† which indicates the superiority of NC@Co(OH)F/CoP<sub>2</sub>/NF toward HER performance in alkaline natural seawater.

To investigate the morphological and structural changes of NC@Co(OH)F/CoP<sub>2</sub>/NF during the HER process, XRD, SEM, and XPS were tested on the catalyst after 3000 CV cycles. As shown in Fig. S9,† the XRD patterns of NC@Co(OH)F/CoP<sub>2</sub>/NF before and after 3000 CV cycles testing indicate that there is no peak position change before and after cycling. The intensity of the diffraction peaks corresponding to CoP<sub>2</sub> decreases after the CV cycles, which may be induced by the partial dissolution of CoP<sub>2</sub> in the catalyst during the electrolysis. However, the diffraction peaks corresponding to Co(OH)F remain visible, suggesting the high structural stability of Co(OH)F during the HER process, contributing to the stability of the catalyst structure. As shown in Fig. S10a and b,† compared to the SEM images of NC@Co(OH)F/CoP<sub>2</sub>/NF before 3000 CV cycles, the catalyst still displays the nanosheet morphology but with a rougher surface (Fig. S10c and d†). The partial fragmentation of the nanosheets occurred during the electrolysis, resulting in the smaller sizes and rougher surfaces of the catalyst. This is attributed to the protective effect of the NC layer and the good stability of the Co(OH)F framework, which provide support and prevent catalyst detachment caused by framework dissolution. As exhibited in Fig. S11a and b,† the high-resolution XPS spectra of C 1s and N 1s show almost no significant changes before and after cycling. There is only a slight decrease in the peak intensity of N 1s, which is caused by the slight dissolution of the external NC layer. In the Co 2p<sub>3/2</sub> spectra (Fig. S11c†) and P 2p spectra (Fig. S11d†), the decrease in the intensity of the corresponding peaks of Co<sup>δ+</sup>, P 2p<sub>3/2</sub> and

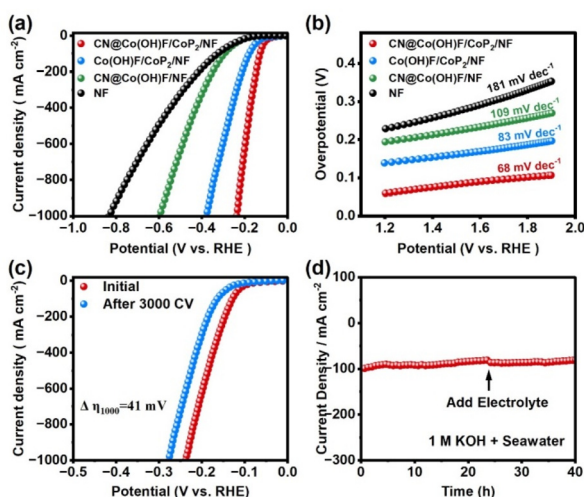


**Fig. 6** HER performance of NC@Co(OH)F/CoP<sub>2</sub>/NF in natural seawater containing 1.0 M KOH. (a) LSV curves of all the reference samples, (b) Tafel plots of different reference samples, (c) LSV curves of NC@Co(OH)F/CoP<sub>2</sub>/NF before and after 3000 CV cycles, and (d) *i*-*t* test of NC@Co(OH)F/CoP<sub>2</sub>/NF at 100 mA cm<sup>-2</sup>.

$P_{2p_{1/2}}$  is related to the partial dissolution of Co–P species during the electrolysis. To confirm the partial dissolution of Co–P species, ICP-OES was used to measure the contents of Co and P in the electrolyte after CV cycling, which the concentration values of Co and P are given in Table S3,† verifying our speculations.

## Conclusions

In summary, a NC-layer-coated Co(OH)F/CoP<sub>2</sub> catalyst NC@Co(OH)F/CoP<sub>2</sub>/NF loaded on nickel foam (NF) was prepared *via* a hydrothermal and phosphorization method. The coupling between the NC layer and CoP<sub>2</sub> facilitates the formation of Co–N bonds, promotes electron transfer, optimizes the overall electronic structure of the catalyst, and the adsorption capacity of the catalyst towards H\* intermediates, thereby improving the catalytic performance. Moreover, the NC layer not only enhances the conductivity of the catalyst but also serves as a protective shell to prevent the agglomeration of CoP<sub>2</sub> during the catalysis process, thus preventing the deactivation of the catalyst. Additionally, the existence of Co(OH)F is conducive to stabilizing the catalyst structure during the HER process. Thus, NC@Co(OH)F/CoP<sub>2</sub>/NF exhibits excellent HER performance in both alkaline fresh water and alkaline natural seawater even at large current densities. This work provided new insights into designing and constructing efficient HER catalysts for application in freshwater and natural seawater.

## Data availability

The data supporting this article has been indicated as part of the ESI.†

## Conflicts of interest

There are no conflicts to declare.

## Acknowledgements

We are thankful for the financial support from NSFC (Grants 21761022, 22162020), the Inner Mongolia Autonomous Region Natural Science Fund project (2024MS02013), and the 2024 Youth Science and Technology Talent Development Project (Young Science and Technology Talents) (NJYT24007).

## References

- 1 M. Vanags, G. Kulikovskis, J. Kostjukovs, L. Jekabsons, A. Sarakovskis, K. Smits, L. Bikse and A. Šutka, *Energy Environ. Sci.*, 2022, **15**, 2021–2028.
- 2 Z. Yuan, J. Tang, D. Chen, Y. Li, Z. Hong and X. He, *Chem. Eng. J.*, 2023, **470**, 144328.
- 3 R.-T. Liu, Z.-L. Xu, F.-M. Li, F.-Y. Chen, J.-Y. Yu, Y. Yan, Y. Chen and B. Y. Xia, *Chem. Soc. Rev.*, 2023, **52**, 5652–5683.
- 4 Y. Liao, G. Deng, H. Wu, L. Ding and H. Wang, *Adv. Funct. Mater.*, 2024, **34**, 2309871.
- 5 Y. Zheng, A. Serban, H. Zhang, N. Chen, F. Song and X. Hu, *ACS Energy Lett.*, 2023, **8**, 5018–5024.
- 6 J. N. Hausmann, R. Schlögl, P. W. Menezes and M. Driess, *Energy Environ. Sci.*, 2021, **14**, 3679–3685.
- 7 Z. Luo, X. Wang, H. Wen and A. Pei, *Int. J. Hydrogen Energy*, 2022, **47**, 24558–24568.
- 8 F. Wu, R. Gao, C. Li and J. Liu, *Energy Convers. Manage.*, 2023, **277**, 116633.
- 9 H. Sun, J. Sun, Y. Song, Y. Zhang, Y. Qiu, M. Sun, X. Tian, C. Li, Z. Lv and L. Zhang, *ACS Appl. Mater. Interfaces*, 2022, **14**, 22061–22070.
- 10 W. Tong, M. Forster, F. Dionigi, S. Dresp, R. Sadeghi Erami, P. Strasser, A. J. Cowan and P. Farràs, *Nat. Energy*, 2020, **5**, 367–377.
- 11 H. Jin, X. Liu, A. Vasileff, Y. Jiao, Y. Zhao, Y. Zheng and S.-Z. Qiao, *ACS Nano*, 2018, **12**, 12761–12769.
- 12 H. Jin, X. Wang, C. Tang, A. Vasileff, L. Li, A. Slattery and S.-Z. Qiao, *Adv. Mater.*, 2021, **33**, 2007508.
- 13 J. Zhu, J. Chi, T. Cui, L. Guo, S. Wu, B. Li, J. Lai and L. Wang, *Appl. Catal., B*, 2023, **328**, 122487.
- 14 L. Sun, Q. Luo, Z. Dai and F. Ma, *Coord. Chem. Rev.*, 2021, **444**, 214049.
- 15 Y. Huang, W. Zhou, W. Kong, L. Chen, X. Lu, H. Cai, Y. Yuan, L. Zhao, Y. Jiang, H. Li, L. Wang, L. Wang, H. Wang, J. Zhang, J. Gu and Z. Fan, *Adv. Sci.*, 2022, **9**, 2204949.
- 16 C. Li, W. Zhang, Y. Cao, J.-Y. Ji, Z.-C. Li, X. Han, H. Gu, P. Braunstein and J.-P. Lang, *Adv. Sci.*, 2024, **11**, 2401780.
- 17 W. Zhang, C. Li, Y. Cao, J.-Y. Ji, Z.-C. Li, Z. Niu, H. Gu, P. Braunstein and J.-P. Lang, *Nano Res.*, 2024, **17**, 3714–3723.
- 18 J.-Y. Xue, F.-L. Li, B. Chen, H. Geng, W. Zhang, W.-Y. Xu, H. Gu, P. Braunstein and J.-P. Lang, *Appl. Catal., B*, 2022, **312**, 121434.
- 19 Z.-Y. Zhao, F.-L. Li, Q. Shao, X. Huang and J.-P. Lang, *Adv. Mater. Interfaces*, 2019, **6**, 1900372.
- 20 C. Li, J.-Y. Xue, W. Zhang, F.-L. Li, H. Gu, P. Braunstein and J.-P. Lang, *Nano Res.*, 2023, **16**, 4742–4750.
- 21 X. Zhang, C. Sun, S. Xu, M. Huang, Y. Wen and X.-R. Shi, *Nano Res.*, 2022, **15**, 8897–8907.
- 22 X. Zhang, X.-R. Shi, P. Wang, Z. Bao, M. Huang, Y. Xu and S. Xu, *Dalton Trans.*, 2023, **52**, 6860–6869.
- 23 R. Liu, L. Chen, F. Mo, H. Song, G. Yang, C. Chen, X. Wu, Y. Huang and Z. Fan, *Chem. Eng. J.*, 2023, **455**, 140545.
- 24 L. Fang, Y. Xie, F. Xu, M. Wang and G. Wang, *Dalton Trans.*, 2023, **52**, 12436–12443.
- 25 N. Jiang, J. Li, B. Wang, Y. Zhang, W. Gao and B. Jiang, *Dalton Trans.*, 2024, **53**, 2048–2054.
- 26 Y. Gao, S. Qian, H. Wang, W. Yuan, Y. Fan, N. Cheng, H. Xue, T. Jiang and J. Tian, *Appl. Catal., B*, 2023, **320**, 122014.
- 27 M. M. Alsabban, M. K. Eswaran, K. Peramaiah, W. Wahyudi, X. Yang, V. Ramalingam, M. N. Hedhili,

- X. Miao, U. Schwingenschlögl, L.-J. Li, V. Tung and K.-W. Huang, *ACS Nano*, 2022, **16**, 3906–3916.
- 28 Y. Zhou, Y. Yang, R. Wang, X. Wang, X. Zhang, L. Qiang, W. Wang, Q. Wang and Z. Hu, *J. Mater. Chem. A*, 2018, **6**, 19038–19046.
- 29 Y. Wang, Y. Jiao, H. Yan, G. Yang, C. Tian, A. Wu, Y. Liu and H. Fu, *Angew. Chem., Int. Ed.*, 2022, **61**, e202116233.
- 30 K. Veeramani, G. Janani, J. Kim, S. Surendran, J. Lim, S. C. Jesudass, S. Mahadik, H. Lee, T.-H. Kim, J. K. Kim and U. Sim, *Renewable Sustainable Energy Rev.*, 2023, **177**, 113227.
- 31 G. Kothandam, G. Singh, X. Guan, J. M. Lee, K. Ramadass, S. Joseph, M. Benzigar, A. Karakoti, J. Yi, P. Kumar and A. Vinu, *Adv. Sci.*, 2023, **10**, 2301045.
- 32 F. M. Yap, J. Y. Loh, S.-F. Ng and W.-J. Ong, *Adv. Energy Mater.*, 2024, **14**, 2303614.
- 33 H. Wu, S. Lu and B. Yang, *Acc. Mater. Res.*, 2022, **3**, 319–330.
- 34 R. Hu, H. Jiang, J. Xian, S. Mi, L. Wei, G. Fang, J. Guo, S. Xu, Z. Liu, H. Jin, W. Xu and J. Wan, *Appl. Catal., B*, 2022, **317**, 121728.
- 35 D. Chen, R. Lu, Y. Yao, D. Wu, H. Zhao, R. Yu, Z. Pu, P. Wang, J. Zhu, J. Yu, P. Ji, Z. Kou, H. Tang and S. Mu, *J. Mater. Chem. A*, 2022, **10**, 7637–7644.
- 36 T. Song, X. Zhang, K. Matras-Postolek and P. Yang, *Carbon*, 2023, **202**, 378–388.
- 37 P. Ding, H. Song, J. Chang and S. Lu, *Nano Res.*, 2022, **15**, 7063–7070.
- 38 Y. Liu, R. Ge, Y. Chen, M. Huang, R. Zhu, W. Li, Y. Liu, L. Feng and R. Che, *Chem. Eng. J.*, 2021, **420**, 127598.
- 39 M. Zhu, S. Yu, R. Ge, L. Feng, Y. Yu, Y. Li and W. Li, *ACS Appl. Energy Mater.*, 2019, **2**, 4718–4729.
- 40 Y. Di, W. Liu, S. Shi, T. Wu, M. Wang and X. Liu, *Chem. Eng. J.*, 2024, **479**, 147589.
- 41 J.-S. Wei, Z.-Y. Zhu, X. Zhao, T.-B. Song, J.-H. Huang, Y.-X. Zhang, X. Liu, L. Chen, X.-Q. Niu, Y.-G. Wang and H.-M. Xiong, *Chem. Eng. J.*, 2021, **425**, 130660.
- 42 H. Wu, Y. Cheng, B. Wang, Y. Wang, M. Wu, W. Li, B. Liu and S. Lu, *J. Energy Chem.*, 2021, **57**, 198–205.
- 43 H. Li, S. Han, B. Lyu, T. Hong, S. Zhi, L. Xu, F. Xue, L. Sai, J. Yang, X. Wang and B. He, *Chin. Chem. Lett.*, 2021, **32**, 2887–2892.
- 44 L. Chen, G. C. Xu, G. Xu and L. Zhang, *Energy Technol.*, 2020, **8**, 1901419.
- 45 Y. Shang, Y. Ding, P. Zhang, M. Wang, Y. Jia, Y. Xu, Y. Li, K. Fan and L. Sun, *Chin. J. Catal.*, 2022, **43**, 2405–2413.
- 46 G.-L. Li, Y.-Y. Miao, F. Deng, S. Wang, R.-X. Wang, W.-H. Lu and R.-L. Chen, *J. Colloid Interface Sci.*, 2024, **667**, 543–552.
- 47 J. Zhang, T. Zhang, J. Ma, Z. Wang, J. Liu and X. Gong, *Carbon*, 2021, **172**, 556–568.
- 48 F. Li, T. Qin, Y. Sun, R. Jiang, J. Yuan, X. Liu and A. P. O'Mullane, *J. Mater. Chem. A*, 2021, **9**, 22533–22543.
- 49 Y. Fan, Y. Zhou, L. Zhang, Y. Feng and K. Shih, *Sep. Purif. Technol.*, 2021, **264**, 118367.
- 50 H. Zhang, H. Li, Y. Zhou, F. Tan, R. Dai, X. Liu, G. Hu, L. Jiang, A. Chen and R. Wu, *J. Energy Chem.*, 2023, **77**, 420–427.
- 51 S. Yoo, Y. Kim, Y. Yoon, M. Karuppannan, O. J. Kwon and T. Lim, *Int. J. Hydrogen Energy*, 2021, **46**, 21454–21461.
- 52 F. Shen, Z. Zhang, Z. Wang, H. Ren, X. Liang, Z. Cai, S. Yang, G. Sun, Y. Cao, X. Yang, M. Hu, Z. Hao and K. Zhou, *Nat. Commun.*, 2024, **15**, 448.
- 53 T. Guo, H. Fei, R. Liu, F. Liu, D. Wang and Z. Wu, *Appl. Catal., B*, 2024, **343**, 123480.
- 54 X. Lv, S. Wan, T. Mou, X. Han, Y. Zhang, Z. Wang and X. Tao, *Adv. Funct. Mater.*, 2023, **33**, 2205161.
- 55 S. Harsha, R. K. Sharma, M. Dierner, C. Baeumer, I. Makhotkin, G. Mul, P. Ghigna, E. Spiecker, J. Will and M. Altomare, *Adv. Funct. Mater.*, 2024, **34**, 2403628.
- 56 M. Moradi, F. Hasanvandian, M. Ghahraman Afshar, A. Larimi, F. Khorasheh, E. Niknam and S. Rahman Setayesh, *Mater. Today Chem.*, 2021, **22**, 100586.
- 57 X. Wu, J. Qiu and Z. Wang, *Small Struct.*, 2023, **4**, 2200268.